Searching for Transient Slow Slips Along the San Andreas Fault Near Parkfield Using Independent Component Analysis

Sylvain Michel, Romain Jolivet, Olivier Lengliné, Adriano Gualandi, Stacy Larochelle, Blandine Gardonio

JGR Solid Earth

RESEARCH ARTICLE
10.1029/2021JB023201

Searching for Transient Slow Slips Along the San Andreas Fault Near Parkfield Using Independent Component Analysis

Sylvain Michel[1], Romain Jolivet[1,2], Olivier Lengliné[3], Adriano Gualandi[4], Stacy Larochelle[5], and Blandine Gardonio[1,6]

[1]Département de Géosciences, Laboratoire de Géologie, PSL Université, CNRS, UMR 8538, École Normale Supérieure, Paris, France, [2]Institut Universitaire de France, Paris, France, [3]École et Observatoire des Sciences de la Terre, UMR7516, Université de Strasbourg / CNRS, Strasbourg, France, [4]Istituto Nazionale di Geofisica e Vulcanologia, Osservatrio Nazionale Terremoti, Roma, Italy, [5]Department of Geology and Planetary Sciences, California Institute of Technology, Pasadena, CA, USA, [6]Laboratoire de Géologie de Lyon, CNRS-Université Lyon 1, Lyon, France

Key Points:

- Independent Component Analysis of GPS time series highlights slip transients along the San Andreas Fault after the 2004 M6 Parkfield event
- We document the spatio-temporal distribution of seismic and aseismic slip history
- Slow Slip Events are more frequent during the 2004 M6 post-seismic period than the subsequent interseismic period

Supporting Information:

Supporting Information may be found in the online version of this article.

Correspondence to:

S. Michel,
sylvain_michel@live.fr

Citation:

Michel, S., Jolivet, R., Lengliné, O., Gualandi, A., Larochelle, S., & Gardonio, B. (2022). Searching for transient slow slips along the San Andreas Fault near Parkfield using independent component analysis. *Journal of Geophysical Research: Solid Earth*, *127*, e2021JB023201. https://doi.org/10.1029/2021JB023201

Received 7 SEP 2021
Accepted 16 MAY 2022

Abstract The Parkfield segment of the San Andreas Fault (SAF) sits at the transition between the locked Cholame segment to the South and the SAF creeping segment to the North. The Parkfield segment hosts regular $\sim M_w 6$ earthquakes followed by postseismic deformation. Recent studies based on geodetic data have highlighted spatial and temporal variations of aseismic slip rate in addition to postseismic slip along this section of the fault. We combine Global Navigation Satellite Systems (GNSS) and seismicity data over the 2006–2018 period to detail a comprehensive picture of transient slip events. We produce a catalog of relocated seismicity and repeating earthquakes. We use a variational Bayesian independent component analysis decomposition on GNSS data to separate geodetic deformation due to non-tectonic sources from signals of potential tectonic origin. We then reconstruct the temporal evolution of fault slip and detect potential slip transients. Those events, determined as mostly aseismic with the exception of one related to a $M_w 4.8$ earthquake, occur more frequently during the 2004 $M_w 6$ post-seismic period than during the subsequent inter-seismic phase. Our study illustrates the rich dynamics of seismic and aseismic slip during both post- and inter-seismic periods along active faults.

Plain Language Summary Faults can slip abruptly, generating earthquakes and seismic waves, or slowly and aseismically. Such a slow motion has now been observed along multiple active faults and is recognized as one of the important processes influencing the Earth's crust stress field. Aseismic slip interacts with earthquakes, and monitoring its time evolution on faults help us in better modeling the seismic cycle. Here we focus our attention on the Parkfield fault segment, sitting along the San Andreas Fault in California in between a section that generated a large earthquake (M7.9) in 1857 and a 150-km-long central creeping section that slips aseismically. We dig in noisy time series of surface displacements measured by GNSS (Global Navigation Satellite System) to detect and model small variations of aseismic slip rate (10–100 mm/year) along the fault. We find multiple candidate slow slip events during the period following the 2004 Parkfield earthquake, confirming and expanding previous independent observations. While aseismic slip following earthquakes was first thought to be a steady release of tectonic stress, we show that, in Parkfield, it is evolving with sudden jumps and slowdown.

1. Introduction

At plate boundaries, interseismic surface strain can be interpreted in terms of fault coupling (i.e., the extent of kinematic locking of a fault) and allows to infer where a fault is prone to release elastic energy through slip, either seismically or aseismically (e.g., Avouac, 2015; Bürgmann, 2018). However, such interpretation does not account for temporal variations in slip rate, though frequently observed in various seismo-tectonic contexts and at different spatial and temporal scales (Jolivet & Frank, 2020, and references therein). Long-term (>1 year) variations of interseismic coupling have been detected in Sumatra, Parkfield and along the Cascadia subduction zone (Barbot et al., 2013; Materna et al., 2019; Tsang et al., 2015). On shorter time scale (<1 year), slow slip events (SSEs) have been observed in areas previously thought to be either locked or slipping continuously, both in subduction zones (e.g., Dragert et al., 2001; Hirose et al., 1999; Michel et al., 2019a) and along strike-slip faults (e.g., Jolivet et al., 2013, Jolivet, Candela, et al., 2015; Khoshmanesh & Shirzaei, 2018a, 2018b; King et al., 1975; Rousset et al., 2016, 2019).

In some regions, the short duration of these transient slip events (days to months) and the associated small surface deformation (mm level) makes them difficult to detect and describe their dynamics (e.g., Cascadia). Furthermore, the relatively short duration of observation periods, from both a geodetic and a seismological perspective, restricts the maximum time-scale over which we can observe such events and ultimately the number of events that we can capture. On the other hand, new methods are being constantly developed to dig into existing data in order to extract increasingly smaller and shorter aseismic slip events along faults, taking advantage of the combination of seismic and geodetic data (e.g., Frank, 2016; Rousset et al., 2019) or of the improvement of geodetic data collection strategies (e.g., Benoit, 2020, PhD thesis; Hussain et al., 2016; Rousset et al., 2016). All these new observations point toward a rich slip dynamics, illuminating the underlying physical processes governing fault slip (Jolivet & Frank, 2020).

We consider a ∼60-km-long section of the San Andreas Fault (SAF) near Parkfield (hereafter referred to as the Parkfield segment) at the transition between the section (hereafter called the Cholame segment) that hosted the M7.8 Fort Tejon earthquake in 1857 (Lienkaemper, 2001; Sieh, 1978; Zielke et al., 2010) and the 150-km-long section that slips aseismically at an average rate of ∼35 mm/yr (Figure 1a; Jolivet, Simons, et al., 2015; Meade & Hager, 2005; Sieh & Jahns, 1984; Titus et al., 2006; Tong et al., 2014). The Cholame segment slipped on average ∼3.5 m during the 1857 Fort Tejon earthquake (Lienkaemper, 2001; Sieh, 1978; Zielke et al., 2012) and is considered locked from the brittle-ductile transition zone to the surface since then. The Parkfield segment is partially locked and hosts ∼M6 earthquakes at least since 1857 with an average recurrence time of 24 ± 9 years (e.g., Jolivet, Simons, et al., 2015; Maurer & Johnson, 2014; Michel et al., 2018; Sieh, 1978; Toppozada & Branum, 2004; Wang et al., 2014). The latest event occurred in 2004 and was followed by postseismic deformation partitioned between afterslip on the fault and deeper (>20 km) viscoelastic relaxation (e.g., Bruhat et al., 2011). Coseismic slip was mainly constrained between 5- and 10-km-depth, potentially extending south within the Cholame segment (Inbal & Ziv, 2020). Afterslip and aftershocks surrounded the coseismic rupture (Figure 1a; e.g., Barbot et al., 2009; Bruhat et al., 2011; Johanson et al., 2006).

In addition to these recurrent earthquakes, transient slow events and seismic activity have been detected along the Parkfield segment of the SAF. Early in 90's, from two-color electronic distance meter, Global Navigation Satellite System (GNSS), creepmeter and strain meter data, a ∼M5.6 SSE spread between October 1992 and December 1994 was detected in Parkfield (Gao et al., 2000; Gwyther et al., 1996; J. R. Murray & Segall, 2005; Langbein et al., 1999; Linde et al., 1996; Nadeau & McEvilly, 1999). This 2-year-long slow slip event, located between 2- and 12-km-depth, was accompanied by an increase in microseismicity. At deeper depths (below 15-km-depth), Rousset et al. (2019) detected transient slip events (∼M4.9) using a geodetic matched filter technique applied on portions of GNSS time series, guided by the occurrence of bursts of low frequency earthquakes detected within continuous seismic records (LFEs; Figure 1b; Frank, 2016; Shelly, 2009, 2017). Based on the spatio-temporal clustering properties of LFEs, Tan and Marsan (2020) estimated M_w1.5–5.1 transient events which shares similar characteristics with earthquakes (e.g., moment-frequency, moment-area and moment-duration scaling laws). At shallower depths, variations of aseismic slip rate were documented between 1993 and 2010 north of Parkfield using Interferometric Synthetic Aperture Radar (InSAR) time series (Bacques et al., 2018; de Michele et al., 2011; Khoshmanesh & Shirzaei, 2018a). The fluctuations of inter-event time of repeating earthquakes (REQs), used as a proxy for slip rate fluctuation, also confirm the occurrence of the 1992 SSE mentioned previously (Nadeau & McEvilly, 1999) and are consistent with the occurrence of transient events in 2008 and 2010 located north of Parkfield (Turner et al., 2015).

It therefore appears that, from depths below the brittle-ductile transition to the surface and over a wide range of temporal scales, from seconds to years, the SAF at Parkfield releases stress repeatedly through slow slip episodes. However, published studies either focused on a single event (e.g., Murray & Segall, 2005), followed closely slip at the surface (0–1 km, Khoshmanesh & Shirzaei, 2018a) or at greater depths (15–30 km, Rousset et al., 2019), but no study has focused on extracting a catalog of slow transient events between the surface and the brittle-ductile transition depth from the noise of existing geodetic time series.

We use daily GNSS and seismicity data over the 2006–2018 period to detail patterns of episodic transient slip. We extract transient slip events that lie hidden within GNSS time series of displacements, using a variational Bayesian Independent Component Analysis (vbICA) decomposition (Gualandi et al., 2016) to separate geodetic deformation due to non-tectonic sources from signals of potential tectonic origin and isolate the signature of transient slip events. This technique has been applied to extract various sources of deformation (SSEs, afterslip,

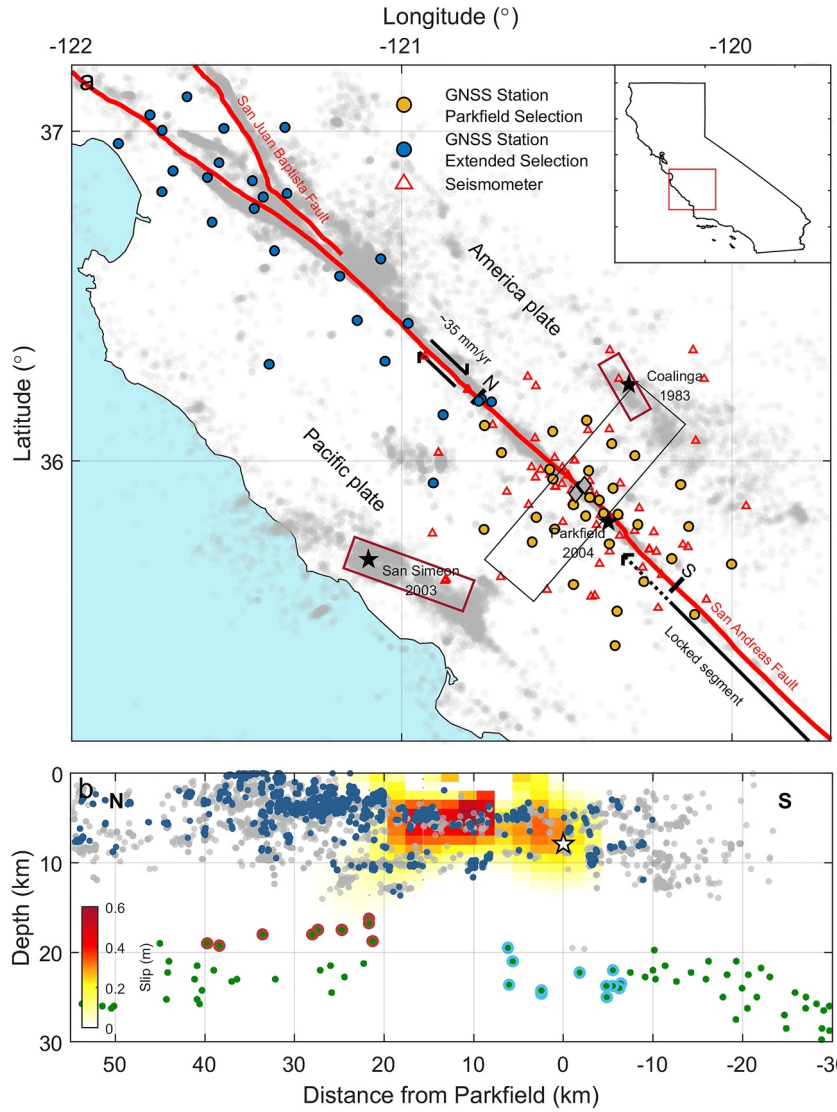

Figure 1. (a) Distribution of Global Navigation Satellite Systems (GNSS) stations (yellow and blue dots) and seismometers (red triangles) along the central section of the San Andreas Fault. All GNSS stations, blue and yellow dots combined, are used to extract the common mode signal (Section 3.2). The GNSS stations indicated by yellow dots are used to extract the tectonic signal from the Parkfield segment (Section 3.3). The GNSS stations CAND and LAND are indicated by gray diamonds. The time series of those stations are shown in Figure 2. The gray dots represent the $M_w > 0.5$ seismicity since 2006 (ComCAT catalog). The black stars indicate the 1983 M_w6.3 Coalinga, 2003 M_w6.6 San Simeon, and 2004 M_w6.0 Parkfield earthquakes epicenter. The red rectangles indicate the rupture extent of the Coalinga and San Simeon earthquakes. The N and S marks indicate the along strike extent of the section in Figure 1b. (b) Co-seismic slip distribution of the 2004 M_w6.0 Parkfield earthquake (modified from Bruhat et al., 2011). The white star indicates its hypocenter (taken from CISN). The gray, blue, and green dots indicate the $M_w > 0.5$ seismicity within 5 km from the SAF since 2006 (ComCAT catalog), repeating earthquakes (Section 2.2) and LFEs location, respectively. The red and blue contours indicate two groups of LFEs that are analyzed in Section 6.2 and Figure 6d.

visco-elastic relaxation, and hydrological deformation) from geodetic time series (Gualandi et al., 2017, 2020; Larochelle et al., 2018; Michel et al., 2019a; Serpelloni et al., 2018). We then invert the tectonic signal for slip on the fault and estimate a time series of moment release rate to identify the main slip events (either seismic or aseismic) over the 2006–2018 time period. We compare the transient, potentially tectonic, events with the micro-seismic activity from an extended REQ catalog of the creeping segment of the SAF and discuss the implication of such transient slip behavior.

In Section 2, we introduce the different data sets used in this study. In Sections 3 and 4, we describe the decomposition of the GNSS signal and the inversion procedure. In Section 5, we explain the detection of the main potential events. In Section 6, we analyze and compare each potential detected event with microseismicity data. Further discussion concludes this study.

2. Data

2.1. GNSS Data

The GNSS data used in this study are taken from the MEaSUREs program, which provides daily position time series acquired by UNAVCO (Network of Americas project) and processed by the Jet Propulsion Laboratory (https://cddis.nasa.gov/archive/GPS_Explorer/archive/, downloaded on 13 September 2019; Noll, 2010). Those time series have been corrected for outliers, and coseismic and non-seismic offsets, and thus correspond to the "Cleaned Trended" product. We select GNSS stations within 25 km of SAF to avoid signal contamination from local anthropogenic sources in the Central Coast and Central Valley. Near Parkfield, most stations have been installed after the M6 earthquake in 2004 and the number of stations is relatively stable from 2006 onwards. We will therefore focus on the 2006–2018 period. We group GNSS sites in two sets of stations. The first set includes stations near the Parkfield segment (yellow dots in Figure 1a) and is used to extract the tectonic signal in this relatively small area ($N_{Parkfield} = 34$ stations, Table S1, in Supporting Information S1). The second set is an extended selection of stations, including sites along the whole central SAF area (yellow and blue dots in Figure 1a). This set covers an area large enough to extract common mode signals from the time series ($N_{Extended} = 61$ stations, Table S1 and S2 in Supporting Information S1).

We only use the horizontal components of the time series (East and North direction) because we expect mostly horizontal tectonic signal related to strike slip along the SAF and because of the high level of noise of the vertical component (approx. 3.5 mm of standard deviation compared to 1.1 mm for the horizontal components). Our data set therefore includes $M_1 = 122$ and $M_2 = 68$ time series for the extended and focused selection, respectively, and the total number of observed epochs is $T = 4{,}502$ (i.e., more than 12 years with daily estimates from 2006 to 2018).

We remove a secular trend to each time series, using a trajectory model accounting for a secular trend, two seasonal terms (annual and semi-annual), and instrumental and co-seismic offsets (Text S1 in Supporting Information S1). For the Parkfield station network (yellow dots in Figure 1), we include an additional term for post-seismic relaxation, defined as an exponential function following the 2004 $M6$ earthquake. Since we begin our analysis in 2006 (2 years after the $M6$ earthquake when the number of stations from the GNSS network is stable), we assume the time series to return, at some point within our observation period, to the average pre-seismic, interseismic rate of motion. Our estimate of the secular trend at each site therefore mostly depends on the later period in our analysis (i.e., after 2011). Figure 2 shows examples of time series before and after detrending. The time series we decompose afterward using vbICA hence include all signals of deformation but the interseismic signal (i.e., the secular trend). Potential slow slip events will appear as deviations from the interseismic rate of motion, similarly to slow slip events in subduction zones (e.g., Materna et al., 2019; 2019a, 2019b).

2.2. Seismicity Data

We use the instrumental seismicity catalog from the ANSS Comprehensive Earthquake Catalog (ComCat) (https://earthquake.usgs.gov/earthquakes/search). We select events from 1984/01/01 up to 2018/12/31, with a minimum magnitude of 0, in the vicinity (<20 km) of the San-Andreas Fault along the Parkfield segment. We relocate 15,247 events using HypoDD double-difference method (Waldhauser & Ellsworth, 2000) with a 3D velocity model of the Parkfield area (Thurber et al., 2006). Events, starting from 2006, are shown in Figure 1b. The magnitude of completeness of events occurring after 2006 is estimated equal to 0.6 using the Maximum curvature method (Wiemer & Wyss, 2000). Those events are then clustered into sequences of repeaters. At the end, 9,680 events are grouped into 1,471 REQ sequences of at least two events, each forming a set of events sharing a similar waveform. REQs, starting from 2006, are shown in Figure 1b. The whole procedure of relocation and event clustering is described in detail in Text S2 in Supporting Information S1.

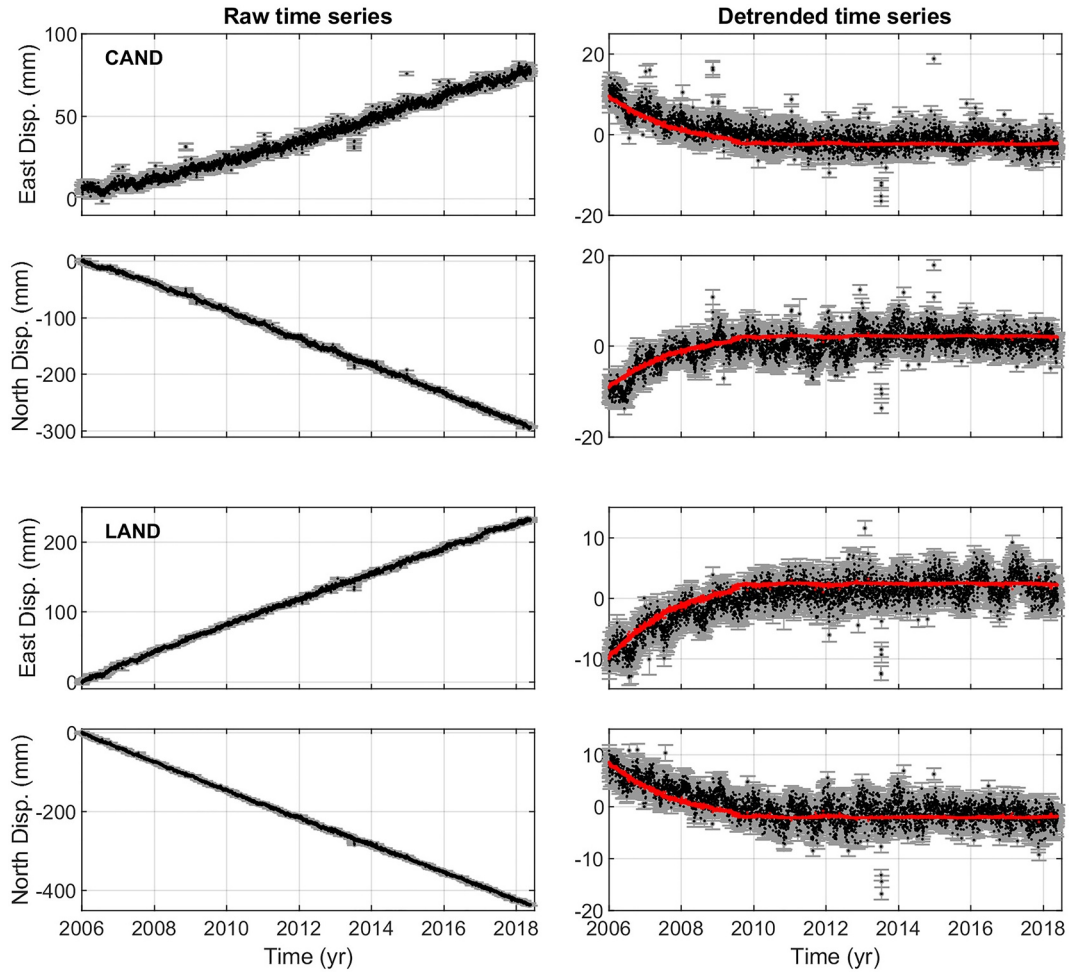

Figure 2. Example of time series before and after removal of the linear trend estimated by a trajectory model (Section 2.1). The black dots and gray error bars indicate the position and their related uncertainty, respectively. Left panels show the raw position time series of stations CAND and LAND (see location on Figure 1). Right panels show their respective time series corrected from the linear trend, and instrumental and coseismic offsets (black dots). The red curve indicates the time series reconstructed from IC1 from Section 3.3.

We directly take the Low Frequency Earthquake catalog from Shelly, 2017. Based on a matched-filter search (Shelly & Hardebeck, 2010) of continuous seismic data (from the High-Resolution Seismic Network), 1,045,627 events were detected from a set of 88 waveform templates. The catalog documents the evolution of LFE activity of 88 families between 2001 and 2016. We isolate two groups of LFE families identified by the green dots with red and light blue contours in Figure 1.

3. Signal Extraction From GNSS Position Time Series

3.1. vbICA Algorithm

We use a signal decomposition technique based on a vbICA (Choudrey & Roberts, 2003; Gualandi et al., 2016) to attempt to separate the deformation signals due to tectonic sources from the non-tectonic ones in the GNSS detrended position time series. We organize the GNSS detrended position time series X_{obs} in a $M \times T$ observation matrix (M is the number of time series and T the number of epochs). We assume that surface displacements result from a limited number of crustal deformation processes L (also referred to as sources), including tectonic (e.g., afterslip, slow slip events) and non-tectonic (e.g., hydrological loading) sources. We further assume that surface displacement is a linear combination of the displacements produced by each source:

$$X_{obs} = A\Sigma + \varepsilon \quad (1)$$

where Σ is the sources matrix, A is the weight of each source (also called mixing matrix), and ε is the noise, here assumed to be zero-mean Gaussian noise. Each row of Σ represents the temporal evolution of a given deformation process. Each column of A represents the spatial distribution associated with a given source. It follows that Σ has size $L \times T$, while A has size $M \times L$.

Just like other multivariate statistical techniques such as PCA, the goal of ICA is to reduce the dimensionality of the dataset. By considering each observed time series as a sample realization of a random variable (rv), that is, considering each row of the X_{obs} matrix as a rv, we attempt extracting L rvs (also referred to as dominant modes or components) to explain the M time series. In other words, we aim to find a reduced number of rvs $L < M$ to represent the original data. The new rvs can be linearly combined to retrieve X_{obs} and are hereafter referred to as Independent Components (ICs) because we use an algorithm that solves the blind source separation problem described in Equation 1 trying to minimize the misfit with the data while keeping the sources in the matrix Σ as much statistically independent as possible.

In particular, we use the variational Bayesian approach described by Choudrey, 2002 to obtain this new set of rvs. Effectively, we use a generative model to model the M-dimensional data with a set of L new rvs, each of these rvs being modeled by a mixture of Gaussian (Choudrey, 2002). Instead of minimizing an approximated version of the mutual information between (or maximizing the negentropy of) the components, we impose the independence in the assumptions of the generative model, introduce an approximating probability density function (pdf) for the model parameter to mimic the true posterior pdf of the model, and try to minimize the dissimilarity between this proxy pdf and the true (unknown) posterior via a variational approach. To do so, the algorithm uses an Expectation-Maximization iterative search that updates the mixtures of Gaussian iteratively. To initialize the model we have to set some hyper-parameters, which control the shape of the described rvs. We use loose a priori hyper-parameters in order to let the algorithm adapt to the data (see Table S3 in Supporting Information S1 for the details). We refer readers to Text S3, as well as Choudrey and Roberts (2003) and Gualandi et al. (2016), for further details on the vbICA technique and its use for geodetic time series analysis.

We highlight here that the temporal evolution associated with each mode or component is not a priori imposed, but extracted from the data to fit the observations while the sources are kept as statistically independent as possible. In this study, for visual purposes, we normalize the components Σ_i between 0 and 1 so that A_i can be interpreted as the spatial pattern of maximum displacement of each component with $i = 1, \ldots, L$.

In terms of interpretation, it is important to note that an ICA seeks to separate statistically independent contributions of stationary sources within the time series data, that is, the mixing matrix does not depend on time and each single independent component has thus a spatial pattern that does not change with time. Consequently, the potentially complex spatiotemporal behavior of a natural process, such as a moving source, will lead the ICA to separate a single physical process into multiple components (Larochelle et al., 2018; Michel et al., 2019), reducing the physical interpretability of the components if taken individually. Additionally, even though vbICA seems an efficient method in separating cleanly sources (Gualandi et al., 2016), cross-talk between independent components remains a possibility.

3.2. Common Mode Signals Extraction

To isolate tectonic signals from the non-tectonic ones, we perform two successive decompositions on our set of observations.

In the first decomposition, we estimate common mode signals, which are displacement signals relatively uniformly distributed across all stations within a given network, often considered to be related to unresolved issues in GNSS processing or large scale seasonal effects such as surface loads and reference frame oscillations (a list of potential sources of seasonal signals can be found in Chanard et al., 2020). We use the extended selection of GNSS stations (yellow and blue dots in Figure 1) to ensure that local tectonic signals of interests will not be included in our estimates of common modes.

The number of extracted components is chosen using the same methodology as Gualandi et al., 2016. Four independent components are needed, and we interpret the first and second as common mode signals: the pattern of displacement of the stations reconstructed by these two components compares to a simple horizontal translation with seasonally modulated amplitude (Figures 3a and 3b). The third component shows the expected post-seismic decay following the 2004, M_w6, Parkfield earthquake (Figure S1 in Supporting Information S1), flattening out in the long-term since the series have been detrended. The fourth seems to be linked to seasonal and multiannual deformation (Figure S1 in Supporting Information S1). We hence correct the initial dataset X_{obs} for the displacement associated with the first two components.

3.3. Tectonic Component Extraction

We then apply the vbICA algorithm to the corrected time series of displacements to isolate sources related to tectonic processes within the Parkfield area. We select only the GNSS stations close to Parkfield (yellow dots in Figure 1) to avoid any contamination of potential sources from the North. The hyper-parameters a priori used for this decomposition are different than the first one (see Text S4 in Supporting Information S1 for discussion and Table S3 in Supporting Information S1). The number of extracted components (10 components) is chosen using a methodology similar to Gualandi et al., 2016. We attribute seven components to either slip on the fault or temporal seasonal variations (Figure 3), while the remaining three components are interpreted as noise (Figure S2 in Supporting Information S1).

Component 1 is clearly related to slip on the fault, characterized by the asymmetric spatial pattern relative to the SAF (Figure 3c). Components 2 and 3 (Figures 3d and 3e) are noisier, but their spatial patterns potentially show asymmetric spatial features to a certain extent (see Figure S3 in Supporting Information S1 for interpretation). Component 4 asymmetric spatial pattern is even less clear, but this component is only active just before the surge in displacement explained also by component 1 and 3 in 2017 (Figure 3f and Figure S3b in Supporting Information S1). We note that the post-seismic relaxation of the 2003 San Simeon earthquake might affect some of the GNSS time series, deviating slightly some components toward San Simeon earthquake epicenter, and we cannot dissociate the 2004 Parkfield postseismic displacements from those of the San Simeon earthquake.

Components 5, 6, and 7 each show a seasonal modulation; hence, we associate these with non-tectonic seasonal sources of deformation (Figures 3g–3i). In order to identify potential physical causes for these seasonally modulated components, in the supplementary material (Text S5 in Supporting Information S1), we compare these three components with the deformation induced by continental water mass variations estimated from satellite gravity records acquired by the Gravity Recovery and Climate Experiment (GRACE) (Larochelle et al., 2018; Tapley et al., 2004). We find that seasonal hydrological loading could explain the behavior of component 5. The origin of the components 6 and 7 are unknown but could possibly arise from other non-tectonic effects which are not explored in this study (e.g., thermal strain (Xu et al., 2017), poro-elastic effects (Jónsson et al., 2003; Nespoli et al., 2018) or more local hydrological processes (e.g., Pintori et al., 2021; Serpelloni et al., 2018). We note that component 7 has to a certain extent an asymmetrical spatial pattern; however, we do not consider it further due to its seasonal temporal behavior.

The other three components retrieved from the second application of the vbICA on GNSS data do not show any spatial or temporal consistency, which leads us to consider these as noise or related to local effects (Figure S2 in Supporting Information S1). These components explain 6% of the time series variance while components 5, 6, and 7 (i.e., seasonal effects) explain 7% of that variance. The components we potentially attribute to slip along the SAF explain 62% of the data variance (see Table S5 in Supporting Information S1).

Component 1 is quite obviously related to tectonic deformation and especially to post-seismic slip. Components 2, 3, and 4 might be as well but are less convincing although we cannot exclude them. Therefore, surface displacements due to slip along the SAF might correspond to any of the eight possible combinations of the components 1 with the remaining 2, 3 and 4. We show in Figure 2 the reconstructed time series for stations CAND and LAND for the sole component 1 while Figure S4 in Supporting Information S1 includes the reconstructed time series for all the stations using all four components. In the following sections we will examine the impact of each component on the detection of transient events.

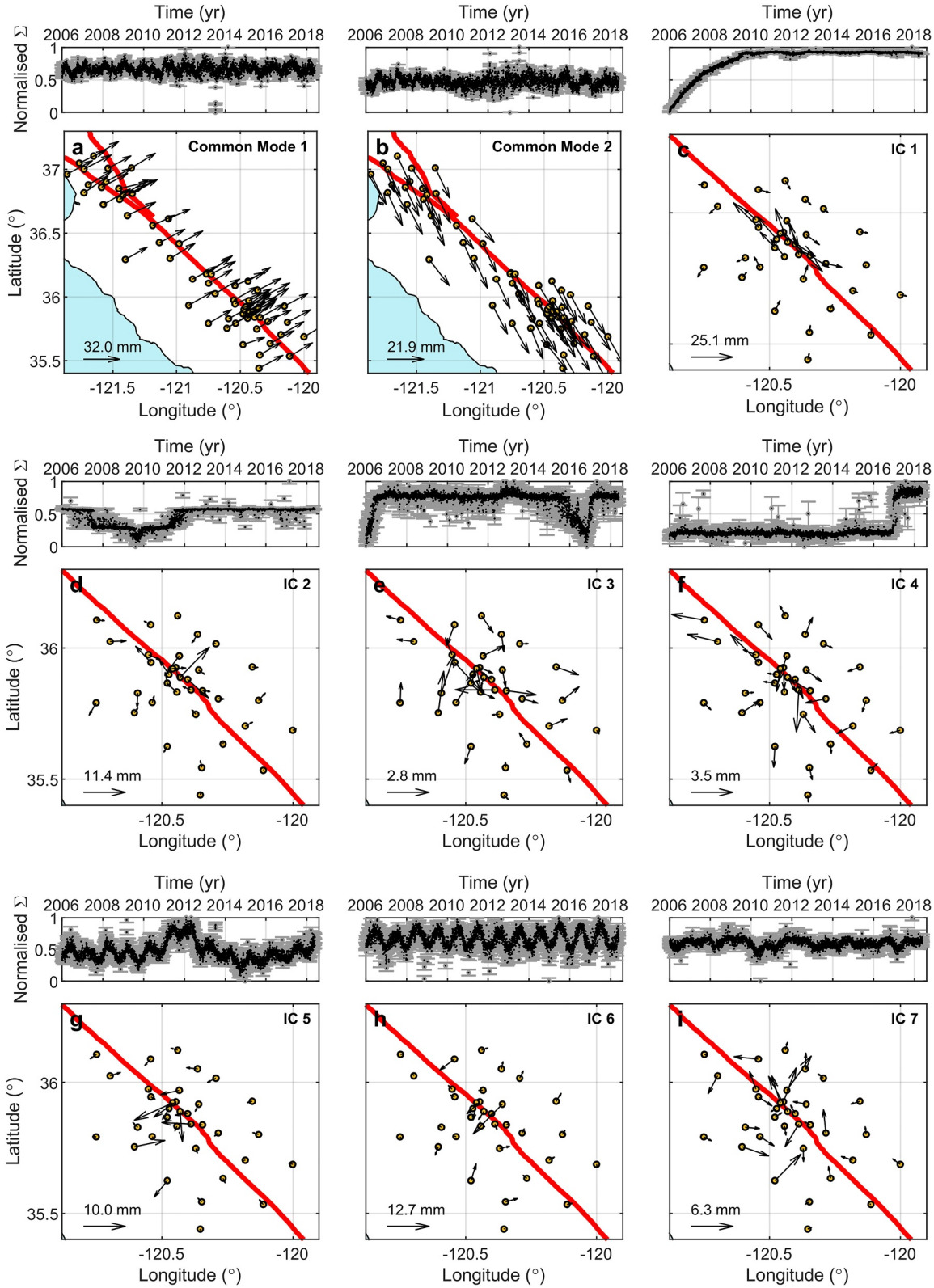

Figure 3.

4. Kinematic Model Inversion

For each of the eight aforementioned scenarios, we model the variations in slip rate, $\dot{\delta}(t)$, relative to the average interseismic slip rate, $\dot{\delta}_i$, over the 2006–2018 time period using the reconstructed time series of displacement. The applied methodology will be the same for each scenario. Variations of slip rate include the post-seismic afterslip following the $M6$ 2004 Parkfield earthquake and potential transient slip during the post-seismic and subsequent interseismic period. As the variations of slip rate we intend to map in space and time are relative to the interseismic slip rate, negative $\dot{\delta}(t)$ corresponds to a decrease in slip rate below the estimated interseismic rate. We build a 3D vertical fault plane discretized in 2×2 km^2 elements following the surface trace of the SAF. Our fault model reaches 20-km-depth, and spans from 30 km south of the $M6$ Parkfield hypocenter to 50 km north of the hypocenter. We calculate displacement rates as the gradient in time of the smoothed displacement time series. The smoothing is done using a zero-phase digital filter with a 20-day window [matlab filtfilt function, with b = ones (1,20)/20 and $a = 1$]. The filter is an averaging sliding window passing through the data in the forward and reverse direction, smoothing periods shorter than ~40 days. We invert the corresponding time series of displacement rate for slip rate at each time step.

Considering the strike slip regime and subvertical dip of the SAF, the potential need to model positive and negative slip rate variations, and the irregular spatial distribution of GNSS stations, the inverse problem is ill-posed. In particular, for a subvertical fault and considering the noise in displacement estimates, comparable surface displacement can be modeled by different depth-dependent distributions of right- and left-lateral slip. We thus enforce slip rate positivity (here, right-lateral slip), a constraint frequently applied when modeling geodetic data (e.g., Jolivet, Simons, et al., 2015; Maurer & Johnson, 2014; Rousset et al., 2016), to reduce the range of possible models to those compatible with the geologic sense of motion of the fault. However, such positivity constraint will result in biases in the inverted slip rate model at periods of slip rate below the interseismic rate. Unlike Gualandi et al., 2017 or Michel et al., 2019, we prefer not to invert the distribution of slip for each independent component and then reconstruct the time series of slip as we cannot translate the positivity constraint to the space defined by the independent components. Therefore, we directly invert for slip at each epoch of the reconstructed time series, enforcing no decrease in slip rate below the interseismic rate.

We compute Green's functions within a semi-infinite homogeneous elastic half-space (Okada, 1992), considering only pure strike slip on the fault. We minimize the least squares cost function, given by,

$$S(m) = \frac{1}{2}\left((\boldsymbol{m}-\boldsymbol{m}_0)^T \boldsymbol{C}_{\boldsymbol{m}}^{-1}(\boldsymbol{m}-\boldsymbol{m}_0) + (\boldsymbol{G}\boldsymbol{m}-\boldsymbol{d})^T \boldsymbol{C}_{\boldsymbol{d}}^{-1}(\boldsymbol{G}\boldsymbol{m}-\boldsymbol{d})\right) \quad (2)$$

where $\boldsymbol{d}$ is the vector of geodetic displacement rate at the surface, $\boldsymbol{G}$ the Green's functions matrix, $\boldsymbol{m}$ is the vector of slip rate on the fault, $\boldsymbol{m}_0$ the prior slip rate model, and $\boldsymbol{C}_{\boldsymbol{d}}$ and $\boldsymbol{C}_{\boldsymbol{m}}$ are the data and model a priori covariance matrices, respectively.

We use the regularization scheme proposed by Radiguet et al., 2011. Our knowledge of the a priori model is described by a multivariate Gaussian PDF centered on the a priori slip rate, $\boldsymbol{m}_0$, with a covariance, $\boldsymbol{C}_{\boldsymbol{m}}$, that depends on the distance between patches:

$$C_{m\,i,j} = \left(\sigma_0 \frac{\lambda}{\lambda_0}\right)^2 \exp\left(-d_{i,j}/\lambda\right) \quad (3)$$

where λ is a characteristic distance, λ_0 is a scaling factor fixed at 2 km (the size of a subfault), σ_0 is the a priori uncertainty on the model parameters, and $d_{i,j}$ is the distance between subfault i and j. We apply a uniform a priori slip rate model of 0 mm/yr, since we are modeling variations of slip rate relative to the interseismic slip rate. λ is set to 2 km (the size of a subfault), while σ_0 is used as a damping parameter. We perform an inversion per time step, but calculate the misfit and norm of the kinematic model over the whole time period for a given σ_0 (See

Figure 3. Spatial and temporal functions of the independent components. Top panels indicate the components temporal evolution (rows of the matrix Σ, Section 3.1), while bottom panels indicate the components spatial pattern (columns of the matrix A, Section 3.1). Red lines are the San Andreas and Calaveras Fault. (a) and (b) are the components related to common mode retrieved on the extended network of GNSS stations (yellow and blue dots in Figure 1) for four components (Section 3.2). Additional components are shown in Figure S1 in Supporting Information S1. (c)–(i) are the components related to tectonic or quasi-seasonal signal retrieved on the focused network of GNSS stations (yellow dots in Figure 1) for 10 components (Section 3.3). Additional components attributed to noise are shown in Figure S2 in Supporting Information S1.

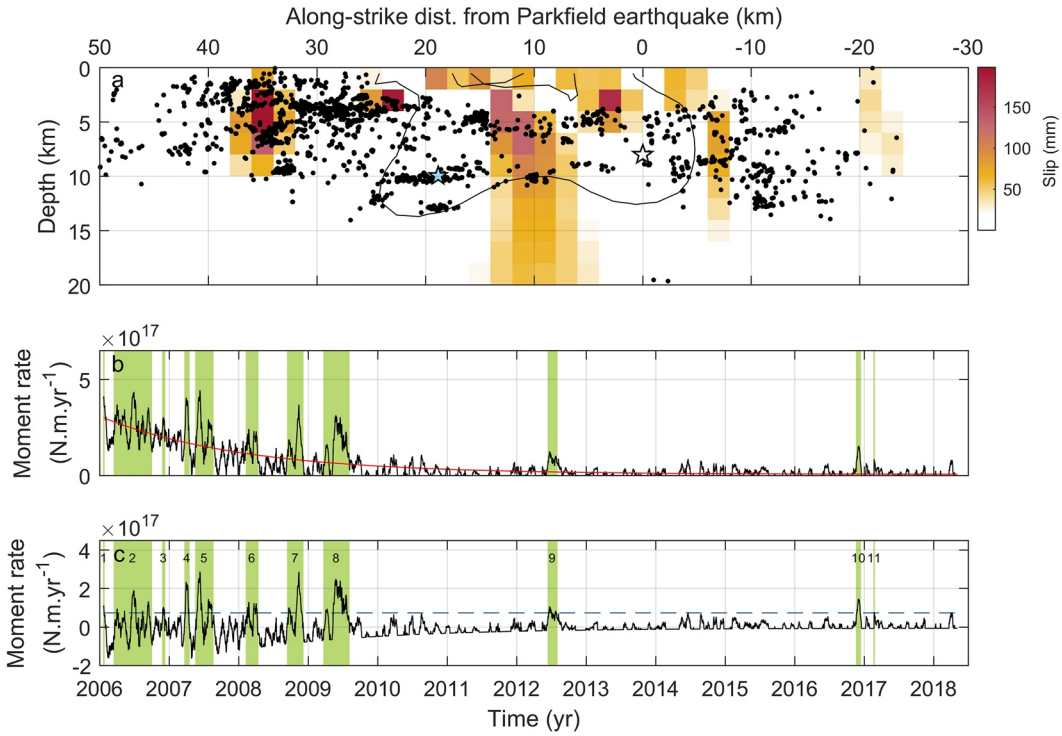

Figure 4. (a) Sum of the slip released during the 11 events identified from IC1 between 2006 and 2018 (see panel (c)). Dark dots are relocated earthquakes. White star is the Parkfield, 2004, M6.0 earthquake hypocenter. Light blue star indicates the location of the main seismic event (M_w4.8) occurring during our observation period. The black line indicates the co-seismic 44 mm slip contour of the 2004 M_w6 earthquake (modified from Bruhat et al., 2011). (b) Moment rate function. The red line represents the idealized postseismic trend estimated using a trajectory model (Text S1 in Supporting Information S1), using only an exponential function to model the post-seismic relaxation. (c) Moment rate function with respect to the interseismic motion and the idealized postseismic signal removed. The blue dashed line indicates the maximum moment rate amplitude between 2014 and 2016 (~4 standard deviation of the moment release rate over this reference period), chosen as the transient detection threshold under the assumption that it is representative of the level of noise in the data. Green shading in (b) and (c) indicates the detected transients.

Text S6 in Supporting Information S1). We chose the optimal value of σ_0 by balancing the Euclidean norm of the model, $||m||_2$, with that of the data misfit (e.g., L-curve plot in Figure S5h in Supporting Information S1). We select σ_0 corresponding to the knee-point of the L-curve, which corresponds to a good tradeoff between misfit and smoothness of the models. Finally, we derive the moment rate release over time along the fault section between −10 and 40 km North of the M6 Parkfield earthquake hypocenter (Figure 4b), as to avoid potential inversion artifacts and edge effects.

The corresponding inversions for each scenario of component combination are shown in panels a and b of Figure S5 to S12 in Supporting Information S1. Likewise, for each scenario, the mean misfit in surface displacement between observations and model at each time step are shown in Figures S5–S12e in Supporting Information S1. Resolution, restitution, and sensitivity maps are shown in Figure S13 in Supporting Information S1 as indicators of the robustness of the inversion. Note that the scenario using only component 1 presents no variation in its spatial pattern of slip except for its amplitude (similar to the one in Figure 4a).

5. Temporal Detection of Transient Slip Events

5.1. Detection Methodology and Results From Independent Component 1

We first focus on the scenario that considers only component 1, which is the sole component for which we are fully confident that it is related to slip on the fault. To first order, we observe a gradual decrease in moment rate until ~2010, consistent with earlier descriptions of the post-seismic transient in Parkfield. In addition, we

observe multiple episodes of slip rate increase in the kinematic model, which we refer to as potential slip events (Figure S5 in Supporting Information S1).

Based on the evolution of the moment rate, we identify the onset and termination of the most obvious slip events over this period. We remove an exponential function from the moment rate evolution and assume that whenever the corrected moment rate exceeds a certain threshold, a slip event is detected (Text S1 in Supporting Information S1, Figures 4b and 4c). We fix the threshold as the maximum moment rate during the 2014–2016 period (~4 times the moment rate standard deviation during the same period), a period assumed with only noise, and extract 30 events. However, several detections are close in time and possibly stem from events that may have been split due to the choice of the threshold and to remaining noise. We therefore merge events less than 20 days apart, a period similar to the width of the temporal filter applied on the data (Section 4). The final catalog of slip events is composed of 11 candidates (Figure 4c). We notice that they correspond to coherent spatial patterns consistent with slip on the SAF, even though potential cross-talk between independent components is still possible. The duration of those events ranges from 1 to 193 days (Table S6 in Supporting Information S1), but those estimates should be taken with care as they are affected by the temporal filter (Section 4) and detection threshold. Note that detected event 1 is timed right at the beginning of the time period and may thus be longer or the choice of the exponential function to mimic the post-seismic slip rate decay may be inaccurate at the beginning of the considered time span.

The early period, 2006–2010, corresponds to the late post-seismic period that followed the 2004 $M6$ Parkfield earthquake (Figure 4b). During this period, we observe significant slip rate variations on top of the usual continuous decay of aseismic slip rate (e.g., Hsu et al., 2006; Perfettini et al., 2010). In particular, we identify seven potential slip events before 2010 (excluding event 1) with magnitudes ranging between M_w4.2 and 4.9. Those magnitude estimates, calculated as the integral of the moment rate over each event, do not include the moment released by the smooth post-seismic trend (Table S6 in Supporting Information S1). Note that the sum of the moment released over an event duration, based on as many inversions as time steps in the considered time span, can potentially lead to constructive noise, leading to an over- or under-estimation of the retrieved magnitude. We evaluate the moment released seismically during these events and find it negligible in comparison to the total moment released retrieved geodetically (Table S6 in Supporting Information S1). We therefore consider these seven events (excluding event 1) as potential slow slip events.

The 2010–2018 period (Figure 4b) is considered as the interseismic period but is nevertheless characterized by three episodes of moment rate increase in mid-2012, end of 2016 and beginning of 2017 (respectively events 9, 10, and 11). Magnitude estimates of events 9 and 10 are 4.5 and 4.4, while event 11 is equivalent to a 3.6 but only over a single day. Comparing with our seismicity catalog, events 10 and 11 are dominantly aseismic whereas event 9 is associated with the largest seismic event present during the 12 years of observation, that is, a M_w4.8 at ~10 km depth. For event 9 in 2012, this discrepancy between the moment estimated geodetically (M_w4.5) and seismically (M_w4.8) is either due to the noise level in the geodetic time series, the magnitude evaluation methodology, or the possibility that the event is also partially described in one or several of the other components retrieved in the ICA (e.g., IC 2–4 in Figure 3).

We estimate the uncertainties of the event detection based on IC1. To do so, similarly to Mandler et al. (2021), we build 100 perturbed displacement time series by adding to each position at each time step a random realization of a Gaussian noise based on the data uncertainties. For each of the 100 time series, we apply our decomposition, inversion of the dominant IC and detection methods. In all cases, events 1–8 are detected, while events 9–11 are less certain (~50% of detection; Figures S14a and S14b in Supporting Information S1).

As we have selected for the time being only one component (IC1), the spatial pattern of slip rate does not change in time. Consequently, we cannot differentiate the spatial pattern of the detected events from the smooth post-seismic spatial distribution. The information of the spatial pattern is potentially included in other components of the ICA.

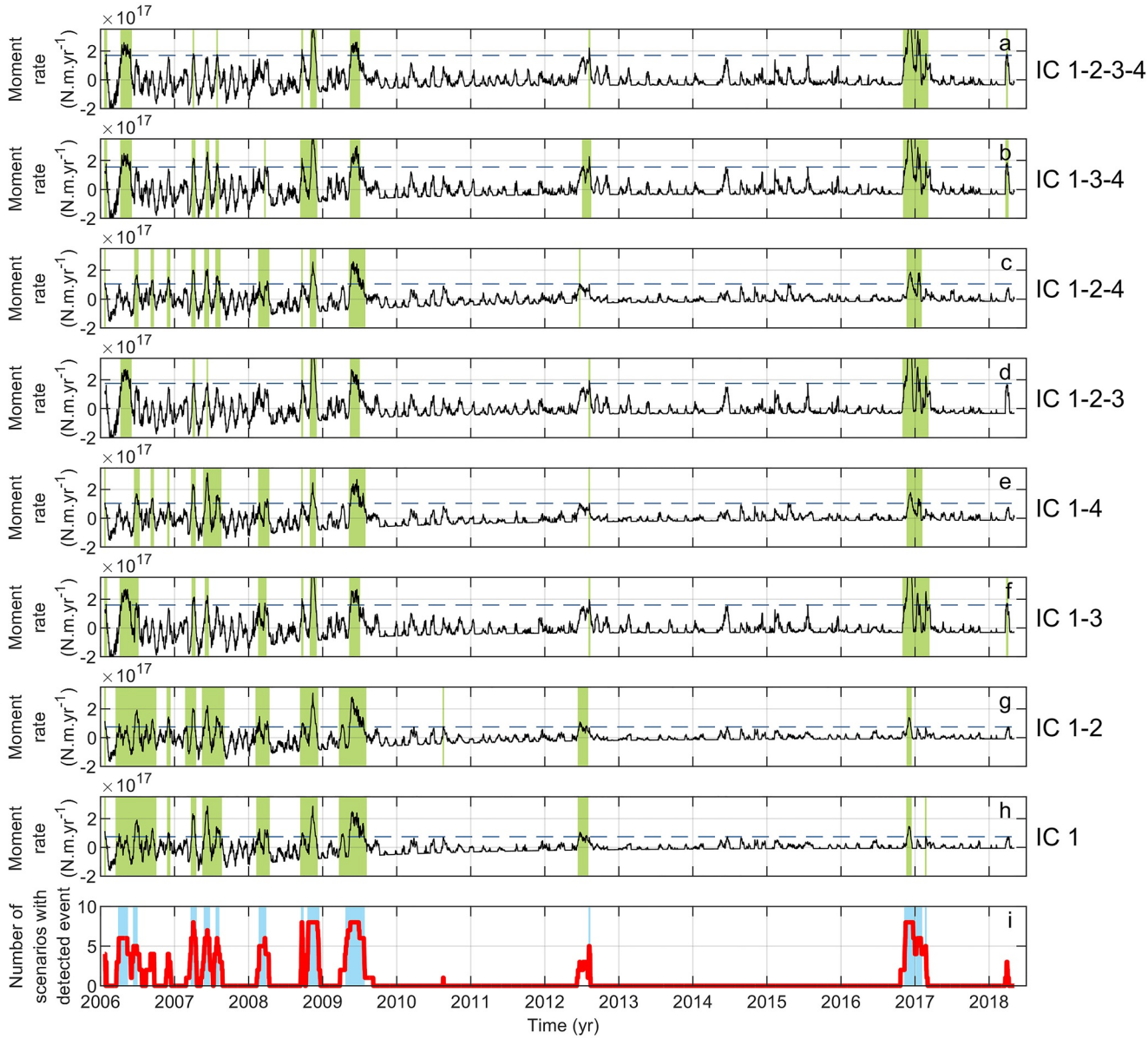

Figure 5. (a)–(h) shows the moment rate function for each of the component combination scenarios. Green shading indicates the detected transients. (i) shows in red for each time step the number of scenarios for which an event is detected. Time steps indicating a detection from more than four scenarios are highlighted in blue, four being the maximum number of scenarios for which component 2, 3, or 4 appears. Those periods highlight the detected events, which are not completely controlled by only one component (component 1 excluded).

5.2. Influence of Independent Components 2, 3, and 4 on the Event Detection Results

We explore whether independent components 2, 3, and 4 (Figure 3; Section 3.3) may contain additional information for some or all of the detected events. We evaluate the evolution of the moment release rate with time considering all possible combinations of the independent components 2, 3, and 4 with component 1.

For instance, comparing the time series reconstructed from component 1 with the time series obtained adding only component 2, we note very little differences in the moment release rate and changes in our detected slip events (Figures 5g and 5h and Figure S14c in Supporting Information S1). Event 11 is not detected anymore, whereas a new event is detected in 2010. The combination of components 1 and 3 infers higher moment rate during the 2006, 2012, and 2016 events (e.g., event 2, 9, and 10; Figure 5f and Figure S14c in Supporting Information S1), but to first order, the resulting detections are similar, with only one additional event detected in 2018.

Finally, component 4 is mostly active beginning of 2017 (Figure 3f) but leads to almost no changes in the moment release rate (Figure 5e and Figure S14c in Supporting Information S1). We evaluate the number of scenarios for which an event is detected at each step of the time series showing that the events detected with the first component only are relatively robust regardless of our choice of the components used for reconstructing the time series (Figure 5i). Including one or several additional components adds noise to the 2014–2016 time period over which we define our detection threshold, consequently impacting the number of detections.

6. Discussion

Using a vbICA, we separate potential tectonic signals from other sources affecting the GNSS position time series such as common mode, surface hydrological loading or local effects. From the four independent components we identified and their combination, we define eight scenarios for which we invert for kinematic models of slip along the SAF near Parkfield between 2006 and 2018. Regardless of the scenario, our results indicate similar slip dynamics to first order, highlighting frequent slip events during the end of the M6 post-seismic period (i.e., until ~2010) in contrast with the subsequent years. We now discuss some of the drawbacks of our procedure and compare our results in light of other datasets. For clarity, note that hereafter the identification of events follows the numbering of the first scenario, using only the first independent component.

6.1. Potential Methodological Limitations

We explore the possibility that other underlying processes or methodological biases may introduce the transient slip events we have detected. For instance, the shallow San Andreas Fault at Parkfield includes multiple parallel strands and treating it as a single fault plane may be problematic (Murray & Langbein, 2006; Simpson et al., 2006). Then, GNSS processing choices (Section 2.1) could possibly also affect the results. However, these are parameters that are out of the scope of the present study and we evaluate the influence of the factors we have some control on.

First, the temporal filter applied in Section 4 could be the origin of the apparent slow slip events between 2006 and 2008, for example (Figure 4b). To rule out this case, we test different smoothing window sizes applied to the time series and observe no shift in time of the transients, suggesting this signal is not related to aliasing of underlying noise (Figures S15 and S16 in Supporting Information S1).

Second, the positivity constraint applied to the slip inversion (Section 5) prevents relocking of the fault, which can be a source of misfit. Such constraint may also potentially affect the detection procedure. In the supplement, we propose a criterion based on the misfit to identify the periods of potential relocking and we show that the detection of the main events remains similar to our conclusions (Text S7; Figure S17 in Supporting Information S1).

Third, the number of events detected in Section 5 is controlled by the detection threshold chosen (maximum moment rate between 2014 and 2016), by the choice of the components to invert for slip on the fault (Figure 5), and to some extent by the smoothing applied for the kinematic model (Figure S15 in Supporting Information S1). The threshold chosen in this study is taken as a conservative value, but one could lower or increase this threshold. An example taking a less conservative detection threshold of three standard deviation is shown in Figure S18 in Supporting Information S1, and results in the detection of 17 events. Such change in detection threshold does not seem to modify the fact that the slow slip events are more frequent during the post-seismic phase of the Parkfield earthquake (<2010) than during the inter-seismic period (>2010).

In addition to all these biases and despite the ICA noise removal approach, the detected events produce only mm scale deformation at the surface (Figures S19–S28 in Supporting Information S1), hence are expected to exhibit noisy displacement fields relatively to the captured displacements. In the supplement, we provide synthetic tests which illustrate the capacity of vbICA to detect a transient based on the GNSS network configuration used in this study (see Text S8 and Figures S29–S32 in Supporting Information S1 for the full results and technical details). On one hand, we find that, once removed the common mode signals, the technique extracts displacement fields with maximum amplitude at the surface of 0.75 mm or above associated with a static source of deformation (Figures S29 and S30 in Supporting Information S1). Such surface displacement were acquired using a synthetic event of multi-variate Gaussian shape centered at a depth of 7 km on the fault, with a variance of 1 km^2 and a maximum cumulative slip of about 30 mm. On the other hand, a synthetic test which produces maximum

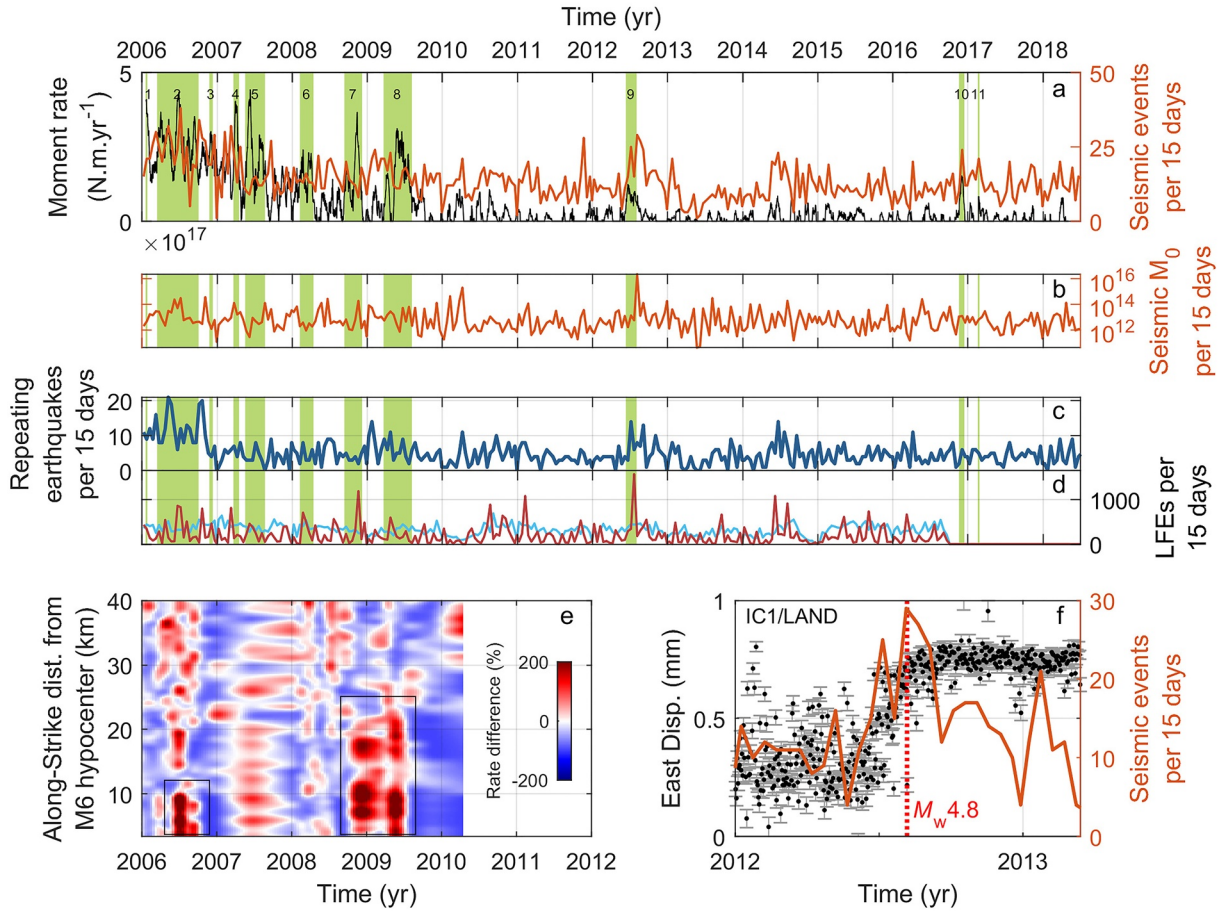

Figure 6. (a) Moment rate function (black) as in Figure 4b. The orange line represents the seismicity rate of events 5 km from the San Andreas Fault (SAF) and within the along-strike [−10, 40] km section. (b) Seismicity moment release rate. (c) and (d) show the repeating earthquake (blue line) and low frequency earthquakes (LFE) (red and light blue line) rate within the along-strike [−10, 40] km section, respectively. The red and light blue lines represent the LFE rate of the families indicated in Figure 1b. (e) Spatiotemporal distribution of rate difference from InSAR data. The relative difference between short-term (between consecutive time steps) and long-term line of sight (LOS) creep rate (slope of the cumulative time series) in percentage (Khoshmanesh & Shirzaei, 2018a). The two black rectangles indicate the slip events as indicated in their paper. (f) Fault parallel displacement time series of GNSS station LAND as reconstructed from IC1 (black dots). The orange line represents the seismicity rate as shown also in (a).

amplitude at the surface of 0.5 mm is considerably more difficult, if not impossible to extract (Text S8 in Supporting Information S1 and Figures S31 and S32 in Supporting Information S1).

6.2. Comparison With Seismicity Data

We now compare the candidate slip events with the micro-seismic activity, occurrences of REQs, and LFEs (Figures 6 and 7). To do so we bin each dataset in time over 15-day windows (Figure 6). Comparison between the candidate transients and creepmeter data are also available in the supplement (Text S9 in Supporting Information S1), as well as a comparison between the slip evolution from the kinematic model and the one derived from REQs (Text S10 in Supporting Information S1).

We observe to first order a gradual decrease in seismicity and repeating earthquake rates (Figure 6a and 6c) consistent with the M_w6 post-seismic decay (i.e., Omori law). More specifically, following the event numbering of scenario using only IC1 (Figure 4c), we observe that events 2, 9, and potentially 10 and 11 in ~2006.5, 2012.5, 2016.9 and 2017.1, respectively, are associated with peaks of seismic activity. However, other events, notably events 7 and 8 in ~ 2008.8 and 2009.4, are not associated with a clear increase of seismicity rate or in the rate of occurrence of REQs. On the other hand, peaks in seismicity rate unrelated to the events we have detected might

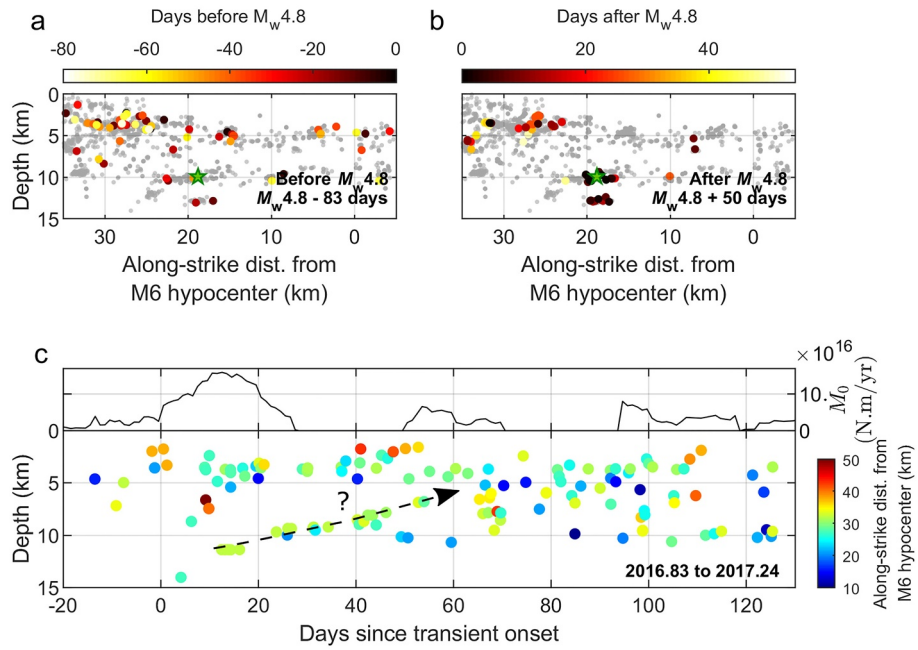

Figure 7. Seismicity distribution during event 9, 10, and 11 in 2012, 2016 and 2017. (a) and (b) show the seismicity distribution before and after the 2012 M_w4.8 earthquake (black star), respectively. Gray dots correspond to the seismicity since 2006, while the colored dots represent the seismicity for the time periods indicated at the bottom right. Note that within the 50 days preceding the M_w4.8 event, 8 M > 0.6 earthquakes occur within 5 km from the M_w4.8 hypocenter. (c) Microseismicity propagation during the 2016–2017 events (Section 6.2), relative to event 10 onset estimated in Section 5.1.

indicate that the seismic signal, and potential underlying aseismic process if any, is too weak to be detected within the geodetic data.

Some of the detected transients, particularly event 7 and 9 in 2008 and 2012, respectively, coincide with LFE surges located north of the M_w6 co-seismic slip (green dots with red contour in Figure 1 and red line in Figure 6d) although LFEs typically highlight deep (>10 km) slip processes. Event 7 in 2008 is associated with high LFE rates (Figure 6d) but also low seismicity rates (Figure 6a), suggesting slip at depth ($\gtrsim$ 10 km). Event 9 in 2012 coincides with both increased seismicity, mostly around 10 km depth, and LFE activity, suggesting a similar depth for this slip event. We note nevertheless that multiple LFE surges do not coincide with our detection and that the LFEs to the south (green dots with light blue contour in Figure 1) do not show clear fluctuations (light blue line in Figure 6d).

Event 9 in 2012 coincides with the largest seismic event in our catalog (M_w4.8). We observe a transient in the GNSS displacement time series reconstructed from IC1 (Figure 6f) ~7–9 weeks before the M_w4.8, consistent with increasing seismicity rates ~9–11 weeks earlier (Figure 6f and 7a). These observations suggest the initiation of a slow slip event before the M_w4.8, which is then combined with afterslip of the seismic event. The question of the potential triggering of this earthquake by the slow slip event is of course open.

Events 10 and 11 are, on the other hand, concurrent with a potential propagation of seismicity from 10 to 5 km depth shown in Figure 7c, although the link between both processes is unclear. Certain creepmeters are also reacting during this time period (notably station XMM1; Figure S33b in Supporting Information S1), however, rain events (Figures S33d and S33e in Supporting Information S1) occur at the same time and could potentially be at the origin of this signal.

6.3. Modulation of Slow Slip Events by Post-Seismic Stress Decay

All detected potential slip events should be considered as slow slip events (i.e., dominantly aseismic events), except the one in mid-2012 which possibly started as a SSE, and was followed by a M_w4.8 earthquake and its corresponding afterslip. We note that the events in 2006, end of 2008 and beginning of 2009 (i.e., events 2, 7,

and 8 with IC1; Figure 4b) coincide with the 2006 and 2008–2009 events detected with InSAR by Khoshmanesh and Shirzaei (2018a), respectively (Figure 6e). The location of slip between 10 and 15 km North of the M_w6 hypocenter (Figure 4) corresponds to the location of the SSE in the early 90's (Murray & Segall, 2005). The majority of the potentially detected SSEs occur between 2006 and 2010 and these events occur while moment release rate decreases through time, consistent with the M_w6 Parkfield post-seismic relaxation. We also note that the inter-event times of SSEs during the post-seismic period seems shorter than the ones during the inter-seismic period.

Such occurrences of slow slip events during the post-seismic phase of major earthquakes have already been documented, in particular in creepmeter data. Following the Superstition Hills earthquakes in 1987, creepmeter records document the occurrence of shallow slow slip events with inter-event time clearly increasing with the ongoing post-seismic transient (Bilham et al., 1989). Creepmeters also document the occurrence of transient events during the post-seismic phase of the 1973, M 7.6, Luhuo earthquake in Sichuan, China (Zhang et al., 2018), although the evolution of the timing of these transients is not described. Such increase of the SSEs' inter-event time between the post- and inter-seismic period points toward a control of the frequency of occurrence of slow slip events by the underlying dynamics of the post-seismic decay. Given the resolution of the data at our disposal we cannot resolve eventual slip migration. Structural heterogeneities, such as spatial variations of the frictional properties along the fault plane (Wei et al., 2013) or geometrical complexities (Romanet et al., 2018) could explain such dynamics.

7. Conclusion

Our results suggests that the post-seismic relaxation following the 2004 Parkfield M_w6 earthquake is not a smooth, continuous process but includes slow and rapid slip transients aggregated together in space and time. Even though the majority of these events occur during the post-seismic period (2011>), large slow slip events also occur spontaneously during the interseismic period (e.g., potentially the events in 2012 and 2016, or the one in the mid-90's; Murray & Segall, 2005). Considering such transient events might initiate at any time along faults while interseismic loading increases the elastic energy available for slip, post-seismic transients might also be considered as periods during which we expect an increase in slow slip event occurrences.

Data Availability Statement

We use the instrumental seismicity catalogue from the ANSS Comprehensive Earthquake Catalog (ComCat) (https://earthquake.usgs.gov/earthquakes/search/). The seismic waveforms from the network BK (https://doi.org/10.7932/BDSN), BP (https://doi.org/10.7932/HRSN) and NC (https://doi.org/10.7914/SN/NC), were downloaded through IRIS (http://ds.iris.edu/ds/#). The Low Frequency Earthquake catalog is taken directly from Shelly, 2017. The GNSS data were acquired by UNAVCO (Network of Americas project) and processed by the Jet Propulsion Laboratory (https://cddis.nasa.gov/archive/GPS_Explorer/archive/; MEaSUREs program).

Acknowledgments
This study has been funded by the Centre National d'Etudes Spatiales (CNES) postdoctoral fellowship. This project has received funding from the European Research Council (ERC) under the European Union's Horizon 2020 research and innovation program (project Geo-4D, Grant Agreement 758210). RJ acknowledges funding from the Institut Universitaire de France. SM, BG, and RJ acknowledge funding from the Laboratoire de Recherche Commun Yves Rocard (ENS/CEA). AG acknowledges funding from the European Research Council Advanced Grant 835012 (TECTONIC). The calculations were performed using MATLAB. The study complies with FAIR Data standards. We thank Jean-Philippe Avouac for his comments on an early version of the manuscript. We thank the anonymous reviewers and the Associate Editor for insightful comments which helped improve the study substantially.

References

Avouac, J.-P. (2015). From geodetic imaging of seismic and aseismic fault slip to dynamic modeling of the seismic cycle. *Annual Review of Earth and Planetary Sciences*, *43*(1), 233–271. https://doi.org/10.1146/annurev-earth-060614-105302

Bacques, G., de Michele, M., Raucoules, D., Aochi, H., & Rolandone, F. (2018). Shallow deformation of the Fan Andreas Fault 5 years following the 2004 parkfield earthquake (Mw6) combining ERS2 and Envisat InSAR. *Scientific Reports*, *8*(1), 1–10. https://doi.org/10.1038/s41598-018-24447-3

Barbot, S., Agram, P., & DeMichele, M. (2013). Change of apparent segmentation of the San Andreas Fault around Parkfield from space geodetic observations across multiple periods. *Journal of Geophysical Research: Solid Earth*, *118*, 6311–6327. https://doi.org/10.1002/2013JB010442

Barbot, S., Fialko, Y., & Bock, Y. (2009). Postseismic deformation due to the Mw 6.0 2004 Parkfield earthquake: Stress-driven creep on a fault with spatially variable rate-and-state friction parameters. *Journal of Geophysical Research*, *114*(7), 1–26. https://doi.org/10.1029/2008JB005748

Benoit, A. (2020). Towards a continuous monitoring of small-scale surface displacements with radar interferometry: Study of the aseismic behavior along the North Anatolian fault. Retrieved from https://tel.archives-ouvertes.fr/tel-03464685v2/document

Bilham, R. (1989). Surface slip subsequent to the 24 November 1987 Superstition Hills, California, earthquake monitored by digital creepmeters. *Bulletin of the Seismological Society of America*, *79*(2), 424–450.

Bruhat, L., Barbot, S., & Avouac, J. P. (2011). Evidence for postseismic deformation of the lower crust following the 2004 Mw6.0 Parkfield earthquake. *Journal of Geophysical Research*, *116*(8). https://doi.org/10.1029/2010JB008073

Bürgmann, R. (2018). The geophysics, geology and mechanics of slow fault slip. *Earth and Planetary Science Letters*, *495*, 112–134. https://doi.org/10.1016/j.epsl.2018.04.062

Chanard, K., Métois, M., Rebischung, P., & Avouac, J.-P. (2020). A warning against over-interpretation of seasonal signals measured by the Global Navigation Satellite System. *Nature Communications*, *11*(1), 1375. https://doi.org/10.1038/s41467-020-15100-7

Choudrey, R. A. (2002). *Variational methods for Bayesian independent component analysis*. University of Oxford. Retrieved from http://www.robots.ox.ac.uk/~parg/projects/ica/riz/Pubs/thesis.ps.gz

Choudrey, R. A., & Roberts, S. J. (2003). Variational mixture of Bayesian independent component analyzers. *Neural Computation*, *15*(1), 213–252. https://doi.org/10.1162/089976603321043766

De Michele, M., Raucoules, D., Rolandone, F., Briole, P., Salichon, J., Lemoine, A., & Aochi, H. (2011). Spatiotemporal evolution of surface creep in the Parkfield region of the San Andreas Fault (1993–2004) from synthetic aperture radar. *Earth and Planetary Science Letters*, *308*(1–2), 141–150. https://doi.org/10.1016/j.epsl.2011.05.049

Dragert, H., Wang, K., & James, T. S. (2001). A silent slip event on the deeper Cascadia subduction interface. *Science*, *292*(5521), 1525–1528. https://doi.org/10.1126/science.1060152

Frank, W. B. (2016). Slow slip hidden in the noise: The intermittence of tectonic release. *Geophysical Research Letters*, *43*(19), 10125–10133. https://doi.org/10.1002/2016GL069537

Gao, S. S., Silver, P. G., & Linde, A. T. (2000). Analysis of deformation data at Parkfield, California: Detection of a long-term strain transient. *Journal of Geophysical Research*, *105*(B2), 2955–2967. https://doi.org/10.1029/1999JB900383

Gualandi, A., Avouac, J. P., Galetzka, J., Genrich, J. F., Blewitt, G., Adhikari, L. B., et al. (2017). Pre- and post-seismic deformation related to the 2015, Mw7.8 Gorkha earthquake, Nepal. *Tectonophysics*, *714–715*, 90–106. https://doi.org/10.1016/j.tecto.2016.06.014

Gualandi, A., Liu, Z., & Rollins, C. (2020). Post-large earthquake seismic activities mediated by aseismic deformation processes. *Earth and Planetary Science Letters*, *530*, 115870. https://doi.org/10.1016/j.epsl.2019.115870

Gualandi, A., Serpelloni, E., & Belardinelli, M. E. (2016). Blind source separation problem in GPS time series. *Journal of Geodesy*, *90*(4), 323–341. https://doi.org/10.1007/s00190-015-0875-4

Gwyther, R. L., Gladwin, M. T., Mee, M., & Hart, R. H. G. (1996). Anomalous shear strain at Parkfield during 1993-1994. *Geophysical Research Letters*, *23*(18), 2425–2428.

Hirose, H., Hirahara, K., Kimata, F., Fujii, N., & Miyazaki, S. (1999). A slow thrust slip event following the two 1996 Hyuganada earthquakes beneath the Bungo Channel, southwest Japan. *Geophysical Research Letters*, *26*(21), 3237–3240. https://doi.org/10.1029/1999GL010999

Hsu, Y.-J., Rosenzweig, C., Livermore, M., Jones, J. W., Curry, R. B., Boote, K. J., et al. (2006). Frictional afterslip following the 2005. *Environmental Protection*, *312*(June), 1921–1926.

Hussain, E., Hooper, A., Wright, T. J., Walters, R. J., & Bekaert, D. P. S. (2016). Interseismic strain accumulation across the central North Anatolian Fault from iteratively unwrapped InSAR measurements. *Journal of Geophysical Research: Solid Earth*, *121*(12), 9000–9019. https://doi.org/10.1002/2016JB013108

Inbal, A., & Ziv, A. (2020). *Automatic extraction of permanent ground offset from near-field accelerograms: Algorithm, validation, and application to the 2004 Parkfield earthquake* (pp. 1–9). Bulletin of the Seismological Society of America. https://doi.org/10.1785/0120200040

Johanson, I. A., Fielding, E. J., Rolandone, F., & Bürgmann, R. (2006). Coseismic and postseismic slip of the 2004 Parkfield earthquake from space-geodetic data. *Bulletin of the Seismological Society of America*, *96*(4B), 269–282. https://doi.org/10.1785/0120050818

Jolivet, R., Candela, T., Lasserre, C., Renard, F., Klinger, Y., & Doin, M. P. (2015). The burst-like behavior of aseismic slip on a rough fault: The creeping section of the Haiyuan fault, China. *Bulletin of the Seismological Society of America*, *105*(1), 480–488. https://doi.org/10.1785/0120140237

Jolivet, R., & Frank, W. B. (2020). The transient and intermittent nature of slow slip. *AGU Advances*, *1*(1). https://doi.org/10.1029/2019AV000126

Jolivet, R., Lasserre, C., Doin, M.-P., Peltzer, G., Avouac, J.-P., Sun, J., & Dailu, R. (2013). Spatio-temporal evolution of aseismic slip along the Haiyuan fault, China: Implications for fault frictional properties. *Earth and Planetary Science Letters*, *377–378*, 23–33. https://doi.org/10.1016/j.epsl.2013.07.020

Jolivet, R., Simons, M., Agram, P. S., Duputel, Z., & Shen, Z. K. (2015). Aseismic slip and seismogenic coupling along the central San Andreas Fault. *Geophysical Research Letters*, *42*, 297–306. https://doi.org/10.1002/2014GL062222

Jónsson, S., Segall, P., Pedersen, R., & Björnsson, G. (2003). Post-earthquake ground movements correlated to pore-pressure transients. *Nature*, *424*(6945), 179–183. https://doi.org/10.1038/nature01776

Khoshmanesh, M., & Shirzaei, M. (2018a). Episodic creep events on the San Andreas. *Nature Geoscience*, *11*(August), 610–615. https://doi.org/10.1038/s41561-018-0160-2

Khoshmanesh, M., & Shirzaei, M. (2018b). Multiscale dynamics of aseismic slip on central San Andreas Fault. *Geophysical Research Letters*, *45*(5), 2274–2282. https://doi.org/10.1002/2018GL077017

King, G. C. P., Bilham, R. G., Campbell, J. W., McKenzie, D. P., & Niazi, M. (1975). Detection of elastic strainfields caused by fault creep events in Iran. *Nature*, *253*(5491), 420–423. https://doi.org/10.1038/253420a0

Langbein, J., Gwyther, R. L., Hart, R. H. G., & Gladwyn, M. T. (1999). Slip-rate increase at Parkfield in 1993 detected by high-precision EDM and borehole tensor strainmeters. *Geophysical Journal International*, *26*(16), 2529–2532.

Larochelle, S., Gualandi, A., Chanard, K., & Avouac, J. (2018). Identification and extraction of seasonal geodetic signals due to surface load variations. *Journal of Geophysical Research: Solid Earth*, 2018JB016607. https://doi.org/10.1029/2018JB016607

Lienkaemper, J. J. (2001). 1857 slip on the San Andreas Fault Southeast of Cholame, California. *Bulletin of the Seismological Society of America*, *91*(6), 1659–1672. https://doi.org/10.1785/0120000043

Linde, A. T., Gladwin, M. T., Johnston, M. J. S., Gwyther, R. L., & Bilham, R. G. (1996). A slow earthquake sequence on the San Andreas Fault. *Nature*, *383*(6595), 65–68. https://doi.org/10.1038/383065a0

Mandler, E., Pintori, F., Gualandi, A., Anderlini, L., Serpelloni, E., & Belardinelli, M. E. (2021). Post-seismic deformation related to the 2016 Central Italy seismic sequence from GPS displacement time-series. *Journal of Geophysical Research: Solid Earth*, *126*, e2021JB022200. https://doi.org/10.1029/2021JB022200

Materna, K., Bartlow, N., Wech, A., Williams, C., & Bürgmann, R. (2019). Dynamically triggered changes of plate interface coupling in southern Cascadia. *Geophysical Research Letters*, *46*(22), 12890–12899. https://doi.org/10.1029/2019GL084395

Maurer, J., & Johnson, K. (2014). Fault coupling and potential for earthquakes on the creeping section of the central San Andreas Fault. *Journal of Geophysical Research: Solid Earth*, *119*(5), 4414–4428. https://doi.org/10.1002/2013JB010741

Meade, B. J., & Hager, B. H. (2005). Block models of crustal motion in southern California constrained by GPS measurements. *Journal of Geophysical Research B: Solid Earth*, *110*(B03403). https://doi.org/10.1029/2004JB003209

Michel, S., Avouac, J., Jolivet, R., & Wang, L. (2018). Seismic and aseismic moment budget and implication for the seismic potential of the parkfield segment of the San Andreas fault. *Bulletin of the Seismological Society of America*, *108*(1), 19–38. https://doi.org/10.1785/0120160290

Michel, S., Gualandi, A., & Avouac, J.-P. (2019a). Interseismic coupling and slow slip events on the Cascadia megathrust. *Pure and Applied Geophysics*, *176*(9), 3867–3891. https://doi.org/10.1007/s00024-018-1991-x

Michel, S., Gualandi, A., & Avouac, J.-P. (2019b). Similar scaling laws for earthquakes and Cascadia slow-slip events. *Nature*, *574*(7779), 522–526. https://doi.org/10.1038/s41586-019-1673-6

Murray, J., & Langbein, J. (2006). Slip on the San Andreas Fault at Parkfield, California, over two earthquake cycles, and the implications for seismic hazard. *Bulletin of the Seismological Society of America*, *96*(4B), 283–303. https://doi.org/10.1785/0120050820

Murray, J. R., & Segall, P. (2005). Spatiotemporal evolution of a transient slip event on the San Andreas Fault near Parkfield, California. *Journal of Geophysical Research B: Solid Earth*, *110*(9), 1–12. https://doi.org/10.1029/2005JB003651

Nadeau, R. M., & McEvilly, T. V. (1999). Fault slip rates at depth from recurrence intervals of repeating microearthquakes. *Science*, *285*(5428), 718–721. https://doi.org/10.1126/science.285.5428.718

Nespoli, M., Belardinelli, M. E., Gualandi, A., Serpelloni, E., & Bonafede, M. (2018). Poroelasticity and Fluid Flow modeling for the 2012 Emilia-Romagna earthquakes: Hints from GPS and InSAR data. *Geofluids*, 2018, 1–15. https://doi.org/10.1155/2018/4160570

Noll, C. E. (2010). The crustal dynamics data information system: A resource to support scientific analysis using space geodesy. *Advances in Space Research*, *45*(12), 1421–1440. https://doi.org/10.1016/j.asr.2010.01.018

Okada, Y. (1992). Internal deformation due to shear and tensile faults in a half-space. *Bulletin of the Seismological Society of America*, *82*(2), 1018–1040.

Perfettini, H., Avouac, J. P., Tavera, H., Kositsky, A., Nocquet, J. M., Bondoux, F., et al. (2010). Seismic and aseismic slip on the Central Peru megathrust. *Nature*, *465*(7294), 78–81. https://doi.org/10.1038/nature09062

Pintori, F., Serpelloni, E., Longuevergne, L., Garcia, A., Faenza, L., D'Alberto, L., et al. (2021). Mechanical response of shallow crust to groundwater storage variations: Inferences from deformation and seismic observations in the eastern Southern Alps, Italy. *Journal of Geophysical Research: Solid Earth*, *126*, e2020JB020586. https://doi.org/10.1029/2020JB020586

Radiguet, M., Cotton, F., Vergnolle, M., Campillo, M., Valette, B., Kostoglodov, V., & Cotte, N. (2011). Spatial and temporal evolution of a long term slow slip event: The 2006 Guerrero Slow Slip Event. *Geophysical Journal International*, *184*(2), 816–828. https://doi.org/10.1111/j.1365-246X.2010.04866.x

Romanet, P., Bhat, H. S., Jolivet, R., & Madariaga, R. (2018). Fast and slow slip events emerge due to fault geometrical complexity. *Geophysical Research Letters*, *45*(10), 4809–4819.

Rousset, B., Bürgmann, R., & Campillo, M. (2019). Slow slip events in the roots of the San Andreas Fault. *Science Advances*(February), 1–8. https://doi.org/10.1126/sciadv.aav3274

Rousset, B., Jolivet, R., Simons, M., Lasserre, C., Riel, B., Milillo, P., et al. (2016). An aseismic slip transient on the North Anatolian Fault. *Geophysical Research Letters*, *43*(7), 3254–3262. https://doi.org/10.1002/2016GL068250

Serpelloni, E., Pintori, F., Gualandi, A., Scoccimarro, E., Cavaliere, A., Anderlini, L., et al. (2018). Hydrologically induced Karst deformation: Insights from GPS measurements in the Adria-Eurasia plate boundary zone. *Journal of Geophysical Research: Solid Earth*, *123*(5), 4413–4430. https://doi.org/10.1002/2017JB015252

Shelly, D. R. (2009). Possible deep fault slip preceding the 2004 Parkfield earthquake, inferred from detailed observations of tectonic tremor. *Geophysical Research Letters*, *36*(17), 1–6. https://doi.org/10.1029/2009GL039589

Shelly, D. R. (2017). A 15 year catalog of more than 1 million low-frequency earthquakes: Tracking tremor and slip along the deep San Andreas Fault. *Journal of Geophysical Research: Solid Earth*, *122*(5), 3739–3753. https://doi.org/10.1002/2017JB014047

Shelly, D. R., & Hardebeck, J. L. (2010). Precise tremor source locations and amplitude variations along the lower-crustal central San Andreas Fault. *Geophysical Research Letters*, *37*(14). https://doi.org/10.1029/2010GL043672 Crossref Partial Au1 Au2 ATL STL Year Vol Fpage Lpage Iss.

Sieh, K. E. (1978). Slip along the San Andreas Fault associated with the great 1857 earthquake. *Bulletin of the Seismological Society of America*, *68*(5), 1421–1448.

Sieh, K. E., & Jahns, R. H. (1984). Holocene activity of the San Andreas Fault at Wallace Creek, California Holocene activity of the San Andreas Fault at Wallace Creek, California. *The Geological Society of America Bulletin*, *8*, 883–896. https://doi.org/10.1130/0016-7606(1984)95<883

Simpson, R. W., Barall, M., Langbein, J., Murray, J., & Rymer, M. J. (2006). San Andreas Fault geometry in the parkfield, California, region. *Bulletin of the Seismological Society of America*, *96*(4B), S28–S37. https://doi.org/10.1785/0120050824

Tan, Y. J., & Marsan, D. (2020). Connecting a broad spectrum of transient slip on the San Andreas Fault. *Science Advances*, *6*(33), eabb2489.

Tapley, B. D., Bettadpur, S., Ries, J. C., Thompson, P. F., & Watkins, M. M. (2004). GRACE measurements of mass variability in the Earth system. *Science*, *305*(5683), 503–505. https://doi.org/10.1126/science.1099192

Thurber, C., Zhang, H., Waldhauser, F., Hardebeck, J., Michael, A., & Eberhart-Phillips, D. (2006). Three-dimensional compressional wavespeed model, earthquake relocations, and focal mechanisms for the Parkfield, California, region. *Bulletin of the Seismological Society of America*, *96*(4 B), 38–49. https://doi.org/10.1785/0120050825

Titus, S. J., DeMets, C., & Tikoff, B. (2006). Thirty-five-year creep rates for the creeping segment of the San Andreas Fault and the effects of the 2004 Parkfield earthquake: Constraints from alignment arrays, continuous global positioning system, and creepmeters. *Bulletin of the Seismological Society of America*, *96*(4 B), 250–268. https://doi.org/10.1785/0120050811

Tong, X., Smith-Konter, B., & Sandwell, D. T. (2014). Is there a discrepancy between geological and geodetic slip rates along the San Andreas Fault System? *Journal of Geophysical Research: Solid Earth*, *119*, 2518–2538. https://doi.org/10.1002/2013JB010765.Received

Toppozada, T., & Branum, D. (2004). California earthquake history. *Annals of Geophysics*, *47*(2–3), 509–522.

Tsang, L. L. H., Meltzner, A. J., Hill, E. M., Freymueller, J. T., & Sieh, K. (2015). A paleogeodetic record of variable interseismic rates and megathrust coupling at Simeulue Island, Sumatra. *Geophysical Research Letters*, *42*, 10585–10594. https://doi.org/10.1002/2015GL066366.1

Turner, R. C., Shirzaei, M., Nadeau, R. M., & Bürgmann, R. (2015). Slow and Go: Pulsing slip rates on the creeping section of the San Andreas Fault. *Journal of Geophysical Research: Solid Earth*, *120*(8), 5940–5951. https://doi.org/10.1002/2015JB011998

Waldhauser, F., & Ellsworth, W. L. (2000). A double-difference earthquake location algorithm: Method and application to the northern Hayward Fault, California. *Bulletin of the Seismological Society of America*, *90*(6), 1353–1368. https://doi.org/10.1785/0120000006

Wang, L., Hainzl, S., & Zöller, G. (2014). Assessment of stress coupling among the inter-, co-and post-seismic phases related to the 2004 M6 parkfield earthquake. *Geophysical Journal International*, *197*(3), 1858–1868. https://doi.org/10.1093/gji/ggu102

Wei, S., Helmberger, D., & Avouac, J. P. (2013). Modeling the 2012 Wharton basin earthquakes off-Sumatra: Complete lithospheric failure. *Journal of Geophysical Research: Solid Earth*, *118*(7), 3592–3609.

Wiemer, S., & Wyss, M. (2000). Minimum magnitude of completeness in earthquake catalogs: Examples from Alaska, the Western United States, and Japan. *Bulletin of the Seismological Society of America*, *90*(4), 859–869. https://doi.org/10.1785/0119990114

Xu, X., Dong, D., Fang, M., Zhou, Y., Wei, N., & Zhou, F. (2017). Contributions of thermoelastic deformation to seasonal variations in GPS station position. *GPS Solutions*, *21*(3), 1265–1274. https://doi.org/10.1007/s10291-017-0609-6

Zhang, J., Wen, X. Z., Cao, J. L., Yan, W., Yang, Y. L., & Su, Q. (2018). Surface creep and slip-behavior segmentation along the northwestern Xianshuihe fault zone of southwestern China determined from decades of fault-crossing short-baseline and short-level surveys. *Tectonophysics*, *722*, 356–372.

Zielke, O., Arrowsmith, J. R., Ludwig, L. G., & Akciz, S. O. (2012). High-resolution topography-derived offsets along the 1857 Fort Tejon earthquake rupture trace, San Andreas fault. *Bulletin of the Seismological Society of America*, *102*(3), 1135–1154. https://doi.org/10.1785/0120110230

Zielke, O., Arrowsmith, J. R., Ludwig, L. G. S., & Akçiz, S. O. (2010). Slip in the 1857 and earlier large earthquakes along the Carrizo plain. *San Andreas Fault*, *1857*(February), 1119–1123.

References From the Supporting Information

Bakun, W. H. (1984). Seismic moments, local magnitudes and coda-duration magnitudes for earthquakes in central California. *Bulletin of the Seismological Society of America*, *74*(2), 439–458.

Chanard, K., Avouac, J., Ramillien, G., & Genrich, J. (2014). Modeling deformation induced by seasonal variations of continental water in the Himalaya region: Sensitivity to Earth elastic structure. *Journal of Geophysical Research: Solid Earth*, *119*(6), 5097–5113. https://doi.org/10.1002/2013JB010451

Chanard, K., Fleitout, L., Calais, E., Rebischung, P., & Avouac, J. P. (2018). Toward a global horizontal and vertical elastic load deformation model derived from GRACE and GNSS station position time series. *Journal of Geophysical Research: Solid Earth*, *123*(4), 3225–3237. https://doi.org/10.1002/2017JB015245

Eshelby, J. D. (1957). The determination of the elastic field of an ellipsoidal inclusion, and related problems. *Proceedings of the Royal Society of London. Series A. Mathematical and Physical Sciences*, *241*(1226), 376–396.

Gias, G. (2022). Phase randomization. MATLAB Central File Exchange Retrieved from https://www.mathworks.com/matlabcentral/fileexchange/32621-phase-randomization

Hyvärinen, A., & Oja, E. (1997). A fast fixed-point algorithm for independent component analysis. *Neural Computation*, *9*(7), 1483–1492. https://doi.org/10.1162/neco.1997.9.7.1483

Nadeau, R. M., & Johnson, L. R. (1998). Seismological studies at parkfield VI: Moment release rates and estimates of source parameters for small repeating earthquakes. *Bulletin of the Seismological Society of America*, *88*(3), 790–814.

Prichard, D., & Theiler, J. (1994). Generating surrogate data for time series with several simultaneously measured variables. *Physical Review Letters*, *73*(7), 951–954. https://doi.org/10.1103/PhysRevLett.73.951

Rubin, A. M. (2002). Using repeating earthquakes to correct high-precision earthquake catalogs for time-dependent station delays. *Bulletin of the Seismological Society of America*, *92*(5), 1647–1659. https://doi.org/10.1785/0120010180

Schulz, S. S. (1989). Catalog of Creepmeter Measurements in California from 1966 through 1988 (Vol. *89–650*). https://doi.org/10.3133/ofr89650

Seager, R., Hoerling, M., Schubert, S., Wang, H., Lyon, B., Kumar, A., et al. (2015). Causes of the 2011–14 California drought. *Journal of Climate*, *28*(18), 6997–7024. https://doi.org/10.1175/JCLI-D-14-00860.1

Waldhauser, F., & Schaff, D. P. (2021). A comprehensive search for repeating earthquakes in northern California: Implications for fault creep, slip rates, slip partitioning, and transient stress. *Journal of Geophysical Research: Solid Earth*, *126*(11), e2021JB022495.